Mapping transient electric fields with picosecond electron bunches

Long Chen[a,b], Runze Li[a,b], Jie Chen[a,b], Pengfei Zhu[a,b], Feng Liu[a,b,1], Jianming Cao[a,c], Zhengming Sheng[a,b,d], and Jie Zhang[a,b,1]

[a]Key Laboratory for Laser Plasmas (Ministry of Education) and Department of Physics and Astronomy, Shanghai Jiao Tong University, Shanghai 200240, China; [b]Collaborative Innovation Center of Inertial Fusion Sciences and Applications (CICIFSA), Shanghai Jiao Tong University, Shanghai 200240, China; [c]Physics Department and National High Magnetic Field Laboratory, Florida State University, Tallahassee, FL 32310; and [d]The Scottish Universities Physics Alliance, Department of Physics, University of Strathclyde, Glasgow G4 0NG, United Kingdom

Contributed by Jie Zhang, October 12, 2015 (sent for review April 12, 2015; reviewed by ChiKang Li and David Neely)

Transient electric fields, which are an important but hardly explored parameter of laser plasmas, can now be diagnosed experimentally with combined ultrafast temporal resolution and field sensitivity, using femtosecond to picosecond electron or proton pulses as probes. However, poor spatial resolution poses great challenges to simultaneously recording both the global and local field features. Here, we present a direct 3D measurement of a transient electric field by time-resolved electron schlieren radiography with simultaneous 80-μm spatial and 3.7-ps temporal resolutions, analyzed using an Abel inversion algorithm. The electric field here is built up at the front of an aluminum foil irradiated with a femtosecond laser pulse at 1.9×10^{12} W/cm^2, where electrons are emitted at a speed of 4×10^6 m/s, resulting in a unique "peak–valley" transient electric field map with the field strength up to 10^5 V/m. Furthermore, time-resolved schlieren radiography with charged particle pulses should enable the mapping of various fast-evolving field structures including those found in plasma-based particle accelerators.

electron radiography | transient electric field | laser plasma | temporal resolution | spatial resolution

As a fundamental phenomenon, transient electric fields exist widely in plasma systems, such as those driven by intense lasers and particle beams. Such fields can play an important role in the plasma evolution, which are related to various applications, including plasma-based advanced particle acceleration (1–5), inertial confinement fusion (6), high energy density physics (7), astrophysical phenomena (8), as well as shock physics (9). Because of the difficulties in experimental measurements of the fields, however, they have been studied so far mostly through theoretical models and numerical simulations. Recent advances in time-resolved electron (10–14) and proton (15–19) radiography make it possible to directly monitor the transient electric field (TEF) and transient magnetic field (TMF). Ultrashort monoenergy electron bunches are preferable in accessing the TEFs because they are readily available and compact (20–22). Previous electron probing studies have only delivered limited TEF information. For example, electron shadow imaging provides only a profile of the electric field (10–12). By using a probe beam with confined size to improve the spatial resolution, the averaged local electric field is estimated at a given probing distance only (23–25).

Here, we report a picosecond-time-resolved electron schlieren radiography (PESR) that directly maps globally the detailed 3D distribution of the TEFs in a dynamical plasma system, which is usually difficult to obtain with an optical probe. In optical schlieren photography, an optical image is modulated due to the inhomogeneity of local optical paths, which mostly results from the changes of optical refractive index induced by density variations. However, in time-resolved electron schlieren radiography, the probing particle beam is deflected by local electromagnetic fields in laser plasmas, forming a modulated pattern. The TEF and TMF can be measured separately by changing the imaging geometry of the probe beam with respect to the foil surface (13, 19). Because the TMF is very weak due to the low intensity of the pump laser beam and the electron probe propagates along the foil surface in this study, the deflection of the electrons is dominated by TEF. In our experiments, the laser plasma and related TEFs were generated by irradiating a femtosecond laser pulse onto a 2-μm-thick aluminum foil at an intensity of 1.9×10^{12} W/cm^2.

By inserting a grid to divide the probing electron beam into an array of electron beamlets, as shown in Fig. 1 and *Methods*, the grid PESR presented here can trace the deflection of each beamlet and yield a spatially resolved schlieren-type pattern. This provides a means to map the 3D distribution of the TEF with a subhundred-micrometer spatial resolution and a several-picosecond temporal resolution, which could not be accessed in previous studies. The structural and temporal evolution of the TEF is visualized with the time-resolved electron schlieren images (Fig. 2) at different time delays (T) following laser irradiation obtained by the picosecond electron beamlets.

Before laser irradiation ($T = -2$ ps, Fig. 2*A*), the beamlet array is undisturbed and the image is similar to that obtained without illumination. After irradiation, the aluminum surface is ionized through multiphoton and thermal emission processes under our conditions, forming suprathermal electrons. A fraction of the hot electrons escapes from the surface, and results in a redistribution of the residual charges, most of which are neutralized in the few picoseconds following illumination (4, 18). The evolution of the escaped electrons, together with the remaining ions in the foil, contributes to the charge-separated TEF. Thus, the effect of Coulomb scattering that

Significance

Transient electric fields driven by intense lasers and particle beams play a key role in a number of applications from plasma-based particle accelerators to implosion dynamics of inertial fusion targets. Here, a method to map the 3D transient field structures with high resolutions both in time and space by use of picosecond electron bunches is presented. It is applied to measure the transient field evolution induced at a solid surface irradiated by a short pulse laser. This method can be applied to monitor field structures with much higher strength, which may find wide application in relevant research fields.

Author contributions: J. Chen, F.L., and J.Z. designed research; L.C., R.L., P.Z., and F.L. performed research; L.C., R.L., J. Chen, P.Z., F.L., J. Cao, and Z.S. analyzed data; J.Z. proposed the original idea for measuring the transient distribution of the electric fields and provided the overall guidance for the project; and L.C., J. Chen, Z.S., and J.Z. wrote the paper.

Reviewers: C.L., MIT Plasma Science & Fusion Center; and D.N., STFC Rutherford Appleton Laboratory.

The authors declare no conflict of interest.

Freely available online through the PNAS open access option.

[1]To whom correspondence may be addressed. Email: liuf001@sjtu.edu.cn or jzhang1@sjtu.edu.cn.

This article contains supporting information online at www.pnas.org/lookup/suppl/doi:10.1073/pnas.1518353112/-/DCSupplemental.

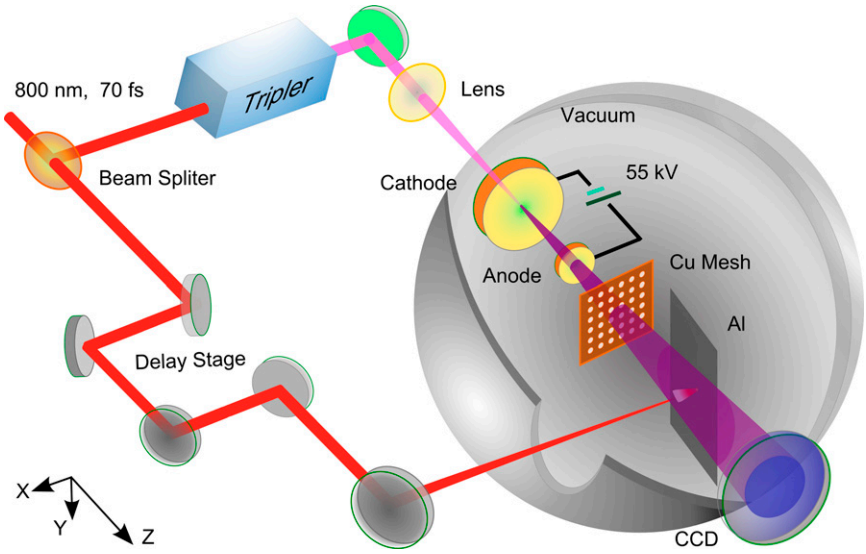

Fig. 1. Schematic diagram of PSER. The optical pump beam irradiates the target at an incident angle of 30° in the *X–Z* plane.

comes from the ions on the probing electrons can be neglected here. As the electrons in the probe beams pass through the TEF region, they are deflected. As a whole, the patterns of the electron beamlets suffer from distortion, which depend upon the time delays as shown in Fig. 2 *C–H*. In the first few picoseconds of laser-induced plasma transformation, the probing electrons that pass the front of the target are strongly repelled from the surface by the escaped electrons. Thus, an electron-depleted hemispherical area is formed, visualized as a hole in the center of Fig. 2*D*. This hole expands as the escaped electrons move outward from the foil surface, as shown in Fig. 2*E*. As delay time increases in Fig. 2 *G* and *H*, the displacement of the row directly over the target surface decreases because of the escaped electrons moving away from the row as well as the TEF weakening in strength.

To map the field distribution, the 2D displacements of the probing electron beamlets at each time delay are obtained by comparing their positions before and after laser irradiation with those depicted in Fig. 3*A*, which are extracted from the corresponding schlieren snapshots. As a representative, the TEF distribution at $T = 25$ ps (Fig. 4 *B–D*) is extracted from the correspondent 2D displacements of beamlets by using the Abel inversion algorithm described in *Methods*. For the electric field component E_x perpendicular to the target surface, we observe a unique "peak–valley" structure on any cross-section along the symmetric axis (the *X* axis), with a demarcation line near $x = 100$ μm where the electric field reverses its direction as shown in Fig. 4*B*. If we denote E_x pointing outward as positive, then the E_x field is 1.2×10^5 V/m at the "peak"

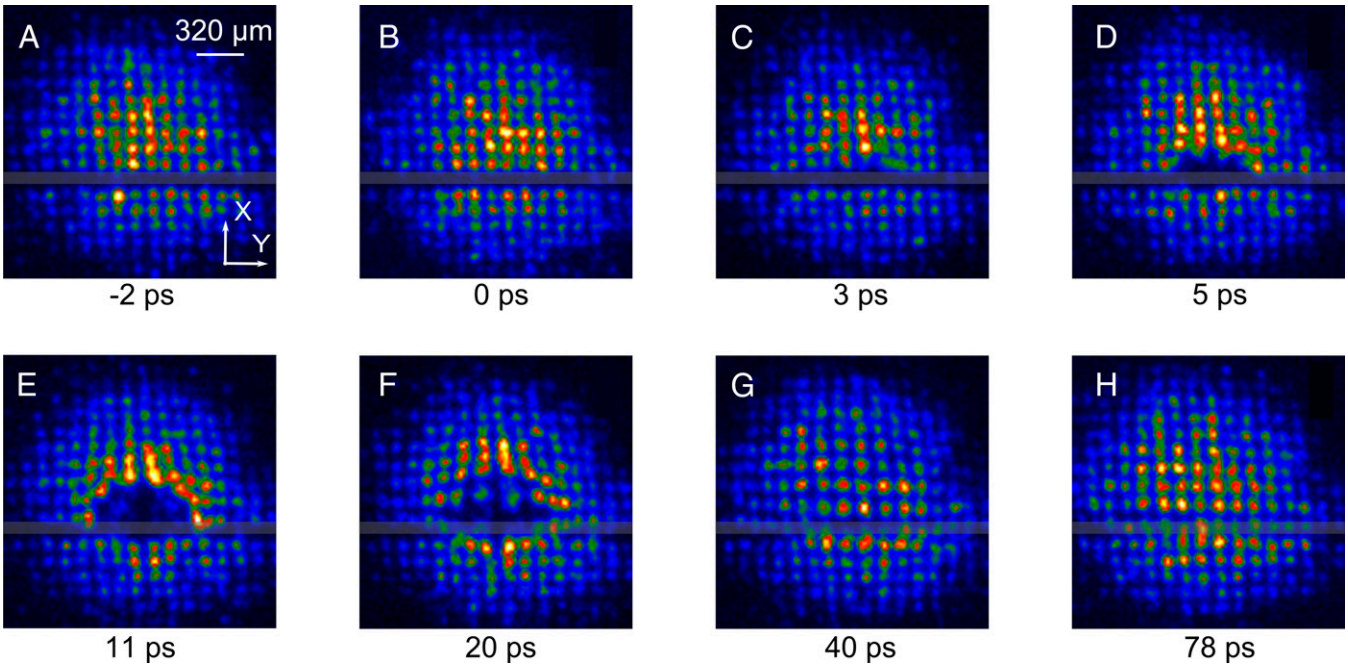

Fig. 2. Snapshots of time-resolved schlieren images at various delay times. *A–H* show the intensity distributions of the probe electron beam after penetrating through the Cu mesh and laser produced plasma at different time delays with the pump laser. Electron intensities in the images are color-coded. The 2-μm foil (at $x = 0$) is marked as a translucent line near the middle of each image.

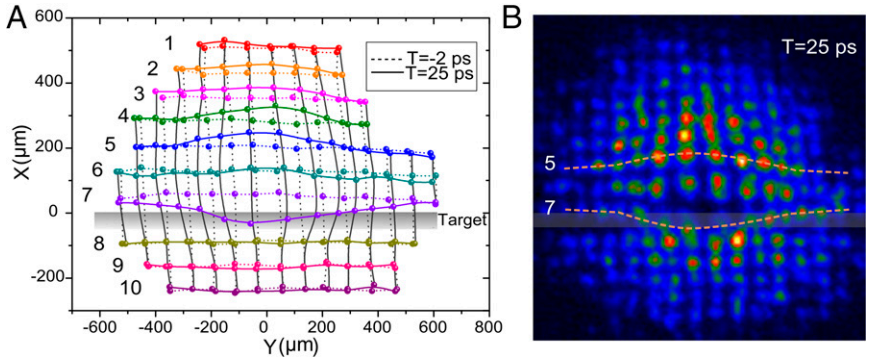

Fig. 3. Positions of electron beamlets. (*A*) Comparison between the positions of the beamlets at T= 25 ps (solid curves) and at T= −2 ps (dotted curves). The position of a beamlet is defined as the coordinates of its centroid mass. (*B*) Raw schlieren image at T = 25 ps. The fifth and seventh rows are marked by dashed curves.

(x = 75 μm) and -9×10^4 V/m at the "valley" (x = 225 μm), approximately. Moreover, when looking into a cross-section of the transverse electric field component E_r parallel to the target surface, it also exhibits the structure of peak and valley. As a result, the total TEF strength as shown in Fig. 4*D* resembles a volcanic crater with negligible value in its interior. Because E_r is zero along the X axis, the on-axis total strength is M-shaped with its two maxima falling on the peak and the valley of E_x, respectively.

Fig. 3 shows the deflections of each beamlet and the snapshot of the PESR image at T = 25 ps. The electron beamlets at the sixth row are barely deflected, which indicates that the TEF strength is approximately zero. Meanwhile the electron beamlets on both sides of the sixth row in Fig. 3 are driven apart due to the opposite E_x directions they experience. The TEF goes to zero (x = ∼100 μm at T = 25 ps) because the emitted hot electrons locate there. Therefore, the average velocity of the emitted hot electrons along the X axis is estimated to be 4×10^6 m/s. Those beamlets, passing the rear of the target, experience a near-zero TEF strength and remain in their original directions as shown by the 8th–10th rows in Fig. 3*A* because of the shields of the residual charges in the foil.

The method described above can be generally extended to different probe beams. For a probing particle with charge Q, rest mass energy ε_0, and kinetic energy ε_k, its deflection angle α along its traveling path in the Z axis can be expressed as

$$\alpha = Q \int_{-\infty}^{+\infty} \frac{E(z)dz}{\varepsilon_k\left(1+\frac{\varepsilon_0}{\varepsilon_0+\varepsilon_k}\right)}, \qquad [1]$$

where $E(z)$ is the electric field at the position z on the trace (*SI Text, Derivation of the Deflective Angle*). Therefore, considering a certain deflection angle (typically several milliradians), the sensitivity to the TEF is mainly determined by the kinetic energy of the probing particle regardless of the sign of its charge. For

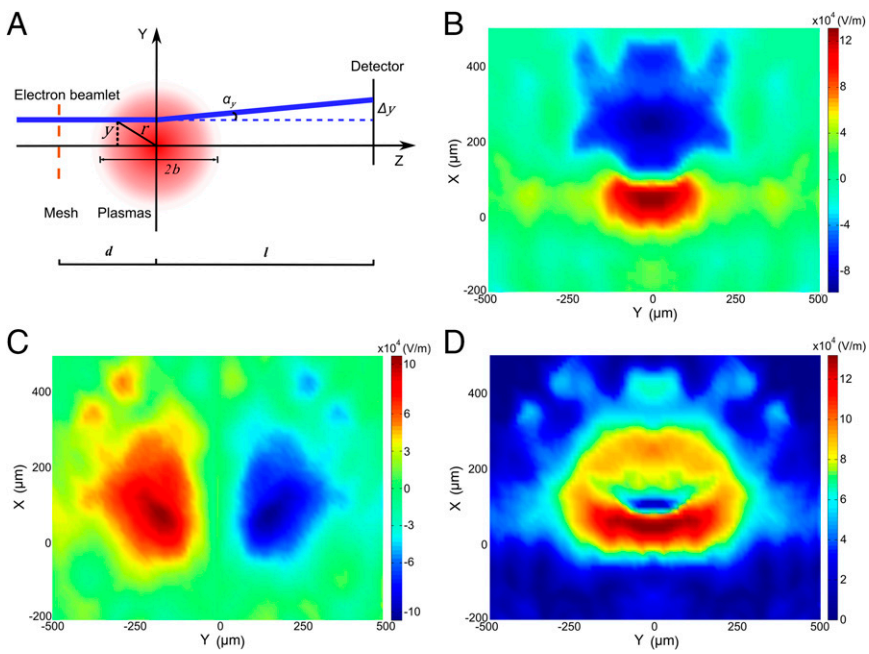

Fig. 4. Schematic diagram of data analysis and the TEF distribution at T = 25 ps. (*A*) The X axis points perpendicularly inward from the target surface and the probing electron beamlets propagate through the laser plasma along the Z axis. Δy is the beam offset past the TEFs induced by laser plasma, and α_y is the corresponding deflection angle. (*B*) $E_x(x, r)$ component. (*C*) $E_r(x, r)$ component. (*D*) The total electric field strength $E = \sqrt{E_x^2 + E_r^2}$. Due to the axial symmetry with respect to the X axis, *B*–*D* actually represent the electric field distribution on any cross-section along the X axis.

example, 15-MeV fusion-reaction–produced protons have been applied to measure TEFs up to 10^8 V/m inside an inertial confinement fusion core (19), whereas 80-keV photoelectrons have shown their adaptability to TEFs within the 10^5-V/m range (24). In principle, time-resolved schlieren radiography can be scaled up to monitor field structures with a much higher strength by increasing the energy of probing particles, either electrons or protons. It is worthy to note that better resolutions of field structures in time and space are ensured by the potentially lower energy spread and shorter bunch length of electrons versus protons. In addition, the electron beams can be generated compactly using different approaches with a wider energy selection range from keV to MeV, providing broader options for transient field diagnostics.

In summary, a scheme to measure the TEF evolution with both spatial and temporal resolutions, respectively, at tens of micrometers and a few picoseconds resolution has been demonstrated. In principle, such ability to capture TEF excitation shall allow for experimental detection of the accelerating-field structures of plasma-based particle accelerators that are driven by intense laser or particle beams (1, 2, 26–28). Time-resolved schlieren radiography may even serve as a means to detect electromagnetic field structures associated with some hydrodynamic instabilities, which are highly detrimental to inertial confinement fusion (29). In such case, the TEFs at a much higher magnitude of 10^9 V/m can be measured quantitatively by increasing the beam energy to tens of MeV.

Methods

PESR. The experimental configuration of the PESR shown in Fig. 1 was modified from the configuration used in previous studies (25, 30) by inserting a thin copper grid at ∼2 mm in front of the target. The probing electron beam has an FWHM diameter of 1.5 mm at the target position with a divergence angle of $\sim 10^{-2}$ radian. The grid preimprints a periodic pattern on the electron beam and splits it into an array of electron beamlets, thus providing a 3D distribution map of the TEFs. Here the spatial resolution is the same as the 80-μm period of the grid with holes separated by ribs of 30-μm width. The resolution could be improved by applying a grid with smaller periods, although it is limited by the uncertainty of the spatial displacement of each electron beamlet, ∼12 μm in this experiment. The overall time resolution in PESR is around 3.7 ps, determined by the optical pump pulse width (t_{pump} = 70 fs), the probing electron bunch length (t_{probe} = ∼2 ps), and its interaction time with the field (t_{inter} = ∼3.1 ps at T = 25 ps). When containing $\sim 3\times 10^3$ electrons per pulse, t_{probe} of the 55-keV electron pulse with an energy spread of 10^{-4} was estimated to be ∼2 ps (31). t_{inter} is defined as $2b/v_z$, where b is the impact parameter (24). At T = 0 ps, b is ∼0.2 mm, therefore t_{inter} equals 3.1 ps with $v_z = 1.29\times 10^8$ m/s at ε_k = 55.0 keV. At later time, the plasma field will cover a larger range due to the expansion of the ejected charge cloud, e.g., at 25 ps to 0.35 mm, the transit time of the electron beam will increase. Thus, the effective time resolution will increase gradually with time. Besides applying a shorter electron pulse, higher temporal resolution can be achieved by increasing the beam energy for shorter interaction time, at the expense of reduction in sensitivity to TEFs. Because the TEF is established instantaneously on arrival of the 70-fs pump laser pulse, we define the moment when the probing electron beam begins deflecting as the time 0, T = 0 ps. Each schlieren image, shown in Fig. 2, was taken by accumulating 10 ultrashort electron pulses to increase signal-to-noise ratio. The irradiated spot on the sample was refreshed every 800 laser shots to avoid potential effects of target damages on the measurement.

Data Analysis Procedure. The TEF distribution at a particular time delay is calculated by performing Abel inversion of the electron schlieren-type radiography data (Fig. 4*A* and *SI Text, Error Analysis*). The axial symmetry of the laser plasma and its associated TEF is visualized by the symmetric beamlet distribution with respect to the X axis at T = 25 ps in Fig. 3*A*, which grounds the application of Abel inversion. We first calculate the components of the deflection angle $\alpha_i(x,y)$ ($i = x, y$) from the displacement of the 55.0-keV probing electron beamlets at the coordinates (x, y) ($Q = -e$, $mv_z^2 = 1.90\varepsilon_k$). The angles $\alpha_i(x,y)$ are linked to the corresponding transient electric field $\boldsymbol{E}(x,y,z) = E_x(x,r)\boldsymbol{e_x} + E_r(x,r)\boldsymbol{e_r}$:

$$\frac{\Delta x}{l} \approx \alpha_x(x,y) = -2\int_y^{+\infty} \frac{eE_x(x,r)}{mv_z^2}\frac{rdr}{\sqrt{r^2-y^2}}, \quad [2]$$

$$\frac{\Delta y}{l} \approx \alpha_y(x,y) = -\int \frac{eyE_r(x,r)}{mr}\frac{dz}{v_z^2} = -2y\int_y^{+\infty} \frac{eE_r(x,r)}{mv_z^2 r}\frac{rdr}{\sqrt{r^2-y^2}}. \quad [3]$$

We then compute the 3D field strengths $E_x(x,r)$ and $E_r(x,r)$ using the Abel inversion (32) as follows:

$$E_x(x,r) = \frac{1}{\pi}\int_r^{+\infty} \frac{mv_z^2}{e}\frac{d\alpha_x(x,y)}{dy}\frac{dy}{\sqrt{y^2-r^2}}, \quad [4]$$

$$E_r(x,r) = \frac{r}{\pi}\int_r^{+\infty} \frac{mv_z^2}{e}\frac{d\frac{\alpha_y(x,y)}{y}}{dy}\frac{dy}{\sqrt{y^2-r^2}}. \quad [5]$$

The data analysis method used in this study can also be applied to proton radiography.

ACKNOWLEDGMENTS. The authors thank Mr. Yuan-Ling Huang for helpful discussion and language editing. This work was supported in part by the National Basic Research Program of China (Grant 2013CBA01500) and the National Natural Science Foundation of China under Grants 11421064, 11304199, 11220101002, and 11327902. J. Cao acknowledges the support from National Science Foundation Grant 1207252.

1. Tajima T, Dawson JM (1979) Laser electron accelerator. *Phys Rev Lett* 43(4):267–270.
2. Chen P, Dawson JM, Huff RW, Katsouleas T (1985) Acceleration of electrons by the interaction of a bunched electron beam with a plasma. *Phys Rev Lett* 54(7):693–696.
3. Pukhov A, Sheng Z-M, Meyer-ter-Vehn J (1999) Particle acceleration in relativistic laser channels. *Phys Plasmas* 6(7):2847–2854.
4. Blumenfeld I, et al. (2007) Energy doubling of 42 GeV electrons in a metre-scale plasma wakefield accelerator. *Nature* 445(7129):741–744.
5. Haberberger D, et al. (2011) Collisionless shocks in laser-produced plasma generate monoenergetic high-energy proton beams. *Nat Phys* 8(1):95–99.
6. Dittrich TR, et al. (1999) Review of indirect-drive ignition design options for the National Ignition Facility. *Phys Plasmas* 6(5):2164–2170.
7. Eliezer S (2002) *The Interaction of High-Power Lasers with Plasmas* (CRC Press, Boca Raton, FL).
8. Li CK, et al. (2013) Structure and dynamics of colliding plasma jets. *Phys Rev Lett* 111(23):235003.
9. Ng A, Ao T, Perrot F, Dharma-Wardana MWC, Foord ME (2005) Idealized slab plasma approach for the study of warm dense matter. *Laser Particle Beams* 23(04): 527–537.
10. Park H, Zuo JM (2009) Direct measurement of transient electric fields induced by ultrafast pulsed laser irradiation of silicon. *Appl Phys Lett* 94(25):251103.
11. Okano Y, Hironaka Y, Kondo KI, Nakamura KG (2005) Electron imaging of charge-separated field on a copper film induced by femtosecond laser irradiation. *Appl Phys Lett* 86(14): 141501.
12. Okano Y, Hironaka Y, Nakamura KG, Kondo KI (2003) Time-resolved electron shadowgraphy for 300 ps laser ablation of a copper film. *Appl Phys Lett* 83(8):1536–1538.
13. Schumaker W, et al. (2013) Ultrafast electron radiography of magnetic fields in high-intensity laser-solid interactions. *Phys Rev Lett* 110(1):015003.
14. Li R-Z, et al. (2014) Investigation of transient surface electric field induced by femtosecond laser irradiation of aluminum. *New J Phys* 16(10):103013.
15. Romagnani L, et al. (2005) Dynamics of electric fields driving the laser acceleration of multi-MeV protons. *Phys Rev Lett* 95(19):195001.
16. Sokollik T, et al. (2008) Transient electric fields in laser plasmas observed by proton streak deflectometry. *Appl Phys Lett* 92(9):091503.
17. Sarri G, et al. (2010) The application of laser-driven proton beams to the radiography of intense laser-hohlraum interactions. *New J Phys* 12(4):045006.
18. Li CK, et al. (2010) Charged-particle probing of x-ray–driven inertial-fusion implosions. *Science* 327(5970):1231–1235.
19. Li CK, et al. (2006) Measuring E and B fields in laser-produced plasmas with monoenergetic proton radiography. *Phys Rev Lett* 97(13):135003.
20. Siwick BJ, Dwyer JR, Jordan RE, Miller RJD (2003) An atomic-level view of melting using femtosecond electron diffraction. *Science* 302(5649):1382–1385.
21. Cao J, et al. (2003) Femtosecond electron diffraction for direct measurement of ultrafast atomic motions. *Appl Phys Lett* 83(5):1044–1046.
22. Wang XJ, Xiang D, Kim TK, Ihee H (2006) Potential of femtosecond electron diffraction using near-relativistic electrons from a photocathode RF electron gun. *J Korean Phys Soc* 48(3):390–396.
23. Li J, et al. (2011) Real-time probing of ultrafast residual charge dynamics. *Appl Phys Lett* 98(1):011501.
24. Li J, et al. (2010) Ultrafast electron beam imaging of femtosecond laser-induced plasma dynamics. *J Appl Phys* 107(8):083305.
25. Zhu P, et al. (2010) Four-dimensional imaging of the initial stage of fast evolving plasmas. *Appl Phys Lett* 97(21):211501.
26. Caldwell A, Lotov K, Pukhov A, Simon F (2009) Proton-driven plasma-wakefield acceleration. *Nat Phys* 5(5):363–367.

27. Mora P (2003) Plasma expansion into a vacuum. *Phys Rev Lett* 90(18):185002.
28. Robson L, et al. (2007) Scaling of proton acceleration driven by petawatt-laser–plasma interactions. *Nat Phys* 3(1):58–62.
29. Li CK, et al. (2013) Observation of strong electromagnetic fields around laser-entrance holes of ignition-scale hohlraums in inertial-confinement fusion experiments at the National Ignition Facility. *New J Phys* 15(2):025040.
30. Zhu PF, et al. (2010) Ultrashort electron pulses as a four-dimensional diagnosis of plasma dynamics. *Rev Sci Instrum* 81(10):103505.
31. Siwick BJ, Dwyer JR, Jordan RE, Miller RJD (2002) Ultrafast electron optics: Propagation dynamics of femtosecond electron packets. *J Appl Phys* 92(3):1643–1648.
32. Li X-F, Huang L, Huang Y (2007) A new Abel inversion by means of the integrals of an input function with noise. *J Phys A Math Theor* 40(2):347–360.